University of Groningen

Spatially distributed patterns of oscillatory coupling between high-frequency amplitudes and low-frequency phases in human iEEG

Maris, Eric; van Vugt, Marieke; Kahana, Michael

IMPORTANT NOTE: You are advised to consult the publisher's version (publisher's PDF) if you wish to cite from it. Please check the document version below.

Document Version
Early version, also known as pre-print

Link to publication in University of Groningen/UMCG research database
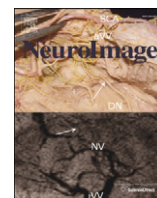
Spatially distributed patterns of oscillatory coupling between high-frequency amplitudes and low-frequency phases in human iEEG

Eric Maris [a,*], Marieke van Vugt [b], Michael Kahana [c]

[a] Donders Institute for Brain Cognition and Behavior, Radboud University, 6525 HR Nijmegen, The Netherlands
[b] Princeton Neuroscience Institute, Green Hall 3-N-11, Princeton, NJ 08540, USA
[c] Department of Psychology, University of Pennsylvania, 3401 Walnut St. Rm 302C, Philadelphia, PA 19104, USA

ARTICLE INFO

ABSTRACT

Spatially distributed coherent oscillations provide temporal windows of excitability that allow for interactions between distinct neuronal groups. It has been hypothesized that this mechanism for neuronal communication is realized by bursts of high-frequency oscillations that are phase-coupled to a low-frequency spatially distributed coupling oscillation. This mechanism requires multiple physiologically different interacting sources, one generating the low-frequency coupling oscillation and the others generating phase-coupled high-frequency oscillations. Using human intracranial EEG (iEEG) data, we provide evidence for multiple oscillatory patterns, as characterized on the basis of their spatial maps (topographies) and their frequency spectra. In fact, we show that the spatial maps for the coupling oscillations are much more widespread than the ones for the associated phase-coupled bursts. Second, in the majority of the patterns of phase-amplitude coupling (PAC), phase-coupled bursts of high-frequency activity are synchronized across brain areas. Third and last, working memory operations affect the PAC strength in a heterogeneous way: in some PAC patterns, working memory operations increase their strength, whereas in others they decrease it.

© 2010 Elsevier Inc. All rights reserved.

Introduction

It is often proposed that oscillations play a central role in the spatiotemporal coordination of neuronal activity (Buzsaki and Draguhn, 2004; Engel et al., 2001; Fries, 2005; Klausberger and Somogyi, 2008; Schroeder and Lakatos, 2009; Varela et al., 2001). The central idea is that spatially distributed coherent oscillations provide temporal windows of excitability that allow for interactions between distinct neuronal groups. One way in which these interactions can occur involves coupled oscillations of different frequencies (Jensen and Colgin, 2007). In this pattern of neuronal activity, the time-varying amplitude of a high-frequency oscillation is phase-coupled to a low-frequency oscillation (phase-amplitude coupling, or PAC). In the following, periods with high amplitude in some high-frequency range will be called *bursts*. If these bursts are coupled to the phase of some low-frequency oscillation, then this latter oscillation will be called a *coupling oscillation*, and the bursts are said to be *phase-coupled* to this coupling oscillation. In Fig. 1, we show simulated field potentials with bursts of gamma oscillations (60 Hz) that are phase-coupled to the rising phase of a theta oscillation (5 Hz). Similar

patterns of cross-frequency interactions have been observed in rats (Chrobak et al., 2000; Sirota et al., 2008; Tort et al., 2008), cats (Schanze and Eckhorn, 1997; von Stein et al., 2000), monkeys (Lakatos et al., 2008, 2005; Schanze and Eckhorn, 1997), and humans (Bruns and Eckhorn, 2004; Canolty et al., 2006; Mormann et al., 2005; Schack et al., 2002). This suggests a form of spatiotemporal coordination in which low-frequency activity, oscillating coherently over multiple neuronal groups, provides the timing information that is required for interactions between distant neuronal groups. This could be implemented in a mechanism that allows local neuronal groups to "listen" to the global low-frequency oscillation, and to concentrate high-frequency oscillations at an appropriate phase of the global oscillation.

In principle, PAC can be generated by many different patterns of interacting sources. For example, one source of low-frequency activity can be coupled to one or more sources of high-frequency activity. Also, there may be multiple sources of low-frequency activity, each coupled to its own set of sources of high-frequency activity. These patterns have not yet been systematically investigated, and this paper attempts to fill this gap. We analyzed human intracranial EEG (iEEG) recordings from patients that had at least 40 implanted electrodes. With this coverage, it is possible to identify the sources via the electrical potential distribution they generate. That is, through volume conduction, the current that is generated by a particular source is picked up to a different extent by the different electrodes, and this produces a discrete spatial map (topography, lead field) that

* Corresponding author. Institute for Brain Cognition and Behavior, Radboud University, 6525 HR Nijmegen, The Netherlands. Fax: +31 24 3616066.
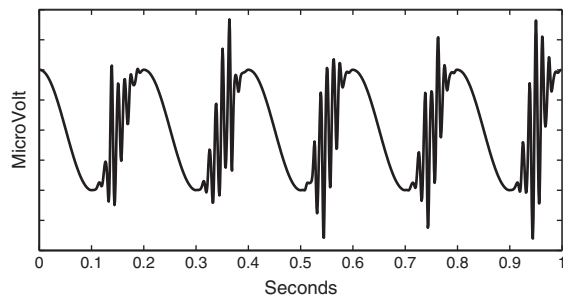E-mail address: e.maris@donders.ru.nl (E. Maris).

Fig. 1. Simulated field potentials with bursts of gamma oscillations (60 Hz) that are phase-coupled to the rising phase of a theta oscillation (5 Hz).

characterizes this source. By means of tensor decomposition (Bro, 1997), we extracted the spatial maps of the sources that are involved in the pattern of PAC. Importantly, this PAC was evaluated for all pairs of different channels, with one channel measuring the low-frequency phase, and the other channel measuring the bursts of high-frequency activity. The pattern of cross-channel PAC provides information about two sets of spatial maps: the spatial maps of the low-frequency coupling oscillations, and the spatial maps of the associated high-frequency phase-coupled bursts. These maps characterize the sources that generate the PAC.

We used these spatial maps to address a serious problem in the empirical identification of PAC, namely that other patterns in the data can easily be misidentified as PAC. For example, Kramer et al. (2008) showed that all existing PAC measures produce erroneous values if a single source produces a rhythmic signal of which the repeating waveform has sharp edges (e.g., interictal spikes). This creates a problem because PAC has been proposed as a mechanism of spatiotemporal integration, which requires multiple interacting sources, one generating a low-frequency coupling oscillation and the others generating phase-coupled bursts of high-frequency activity. In electrophysiological recordings, the signals produced by these two sources are always superimposed. This creates a serious challenge for identifying the coupling between the two, because the two activities have to be separated before one can quantify their coupling strength. This separation requires digital filtering, a technique that can extract any number of band-limited components from the raw electrophysiological recordings, regardless of the number of sources. Importantly, these extracted components may very well exhibit PAC even though only a single source is active, namely if the waveform has sharp edges (Kramer et al., 2008).

We do not attempt to identify the physiological mechanism that produces PAC. However, we do want to make some claims about the source configuration that underlies PAC. To do this, we define a source as activity in the neuronal tissue that is characterized by (1) the spatial map that it produces at the level of the sensors, and (2) its frequency content (spectrum). Not all conceivable physiological mechanisms can be fully described in this way. To appreciate the limits of our approach, in Materials and methods, we give two examples of physiological mechanisms that cannot be fully characterized in terms of a spatial map and a frequency spectrum.

We propose a solution for the problem that repeating waveforms with sharp edges are easily misidentified as PAC. This solution makes use of the two spatial maps that characterize the sources of a pattern of PAC, one for the coupling oscillation and one for the associated phase-coupled bursts. Importantly, if these two spatial maps are identical, then the pattern of PAC may very well be produced by a single source that produces a rhythmic signal with a sharp-edged waveform. On the other hand, if the two spatial maps are different, then they can only be produced by multiple sources. In our study, we found that the spatial maps for the low-frequency coupling oscillations are more widespread than the spatial maps for the high-

frequency phase-coupled bursts. Thus, we found evidence for PAC being produced by multiple sources.

Our analysis of PAC differs from the analyses in most other human iEEG studies (Canolty et al., 2006; Mormann et al., 2005). We analyzed the PAC across all channel pairs, whereas most existing studies analyzed it within the separate channels, with the same channel providing both the low-frequency phases and the bursts of high-frequency activity. As we will show in Results, analyzing cross-channel PAC is essential to be able to separate the spatial maps for the coupling oscillations and the associated phase-coupled bursts. It must be noted that the existence of cross-channel PAC alone does not allow one to conclude that multiple sources are involved in this coupling. In fact, a distributed rhythmic signal with a sharp-edged waveform will result in a significant cross-channel PAC. However, if we observe different spatial maps for the coupling oscillation and the associated phase-coupled bursts, then the cross-channel PAC must be the result of an interaction between different sources.

Our analysis takes as its input a huge four-dimensional array (channels-by-channels-by-frequencies-by-frequencies) of PAC measures, much larger than the one used in the existing studies. In fact, with 40 iEEG channels and 30 frequencies (each indexing both the amplitudes and the phases), we would characterize the PAC with an array of $40 \times 40 \times 30 \times 30 = 1,440,000$ numbers. The analysis of such a huge four-dimensional array requires an approach that identifies structural patterns in this array. We have developed such an approach, based on tensor decomposition (Bro, 1997), and it extracts spatial maps and frequency spectra from this array.

If neuronal information processing occurs during bursts of high-frequency activity, then effective spatiotemporal coordination of neuronal activity can only occur if bursts at different locations occur in overlapping time windows. This type of synchronization could be achieved by a mechanism that concentrates bursts at the same phase of a common coupling oscillation. Using tensor decomposition, we could show that, in the majority of the PAC patterns, the phase-coupled bursts of high-frequency activity are synchronized across brain areas. As will be explained in the following, this synchronization is between amplitude envelopes, and not necessarily between the oscillations of which the amplitudes were calculated.

PAC has been linked to working memory operations. In fact, it has been proposed as the cornerstone of a model for temporal segmentation and integration of items that are kept in working memory (Lisman and Idiart, 1995). This model predicts that theta-gamma PAC is stronger during periods that involve working memory operations than during periods that do not. Inspired by this prediction, we analyzed iEEG recordings that were obtained while the patients performed in a working memory task (Sternberg, 1966). We found that, for some PAC patterns, the coupling strength is modulated by working memory operations.

Materials and methods

Data collection

We analyzed iEEG recordings from 26 patients having implanted electrodes for the purpose of presurgical diagnosis. These were selected from a larger pool of patient data sets, based on the criterion that every data set must have artefact-free recordings from at least 40 grid and/or strip electrodes (see Electrophysiology). Patients volunteered to participate in our cognitive testing in their free time between clinical procedures. The research protocol was approved by the appropriate institutional review boards at the Hospital at the University of Pennsylvania (Philadelphia, PA), Children's Hospital (Philadelphia, PA), University Clinic (Freiburg, Germany), Children's Hospital (Boston, MA), and Brigham and Women's Hospital (Boston, MA). Informed consent was obtained from patients (or their guardians, in the case of children). Some of these data sets have

been examined previously (Jacobs and Kahana, 2009; Raghavachari et al., 2001, 2006; Rizzuto et al., 2003; van Vugt et al., 2010, 2009), but the data analyses described here are novel.

Electrophysiology

The positions of the electrodes were determined by neurologists to identify seizure foci and functional brain regions. Because the clinical procedure of identifying seizure foci involves placing electrodes in any region that is merely potentially epileptogenic, the majority of recordings come from brain regions outside the area that is subsequently determined to be involved in seizures. Recordings were made using grid, strip, and depth electrodes. However, in our analyses, we only used the recordings from the grid and the strip electrodes, which are placed under the dura on the surface of the neocortex.

To determine the electrode locations, a postoperative computed tomography scan was co-registered with a higher-resolution preoperative magnetic resonance image. Every patient's image was normalized to a standard-sized brain, and subsequently Talairach coordinates (Lancaster et al., 2000; Talairach and Tournoux, 1988) were computed. We used brain images from the WFU Pick-Atlas for data visualization (Maldjian et al., 2003).

iEEG activity was recorded at a sampling rate between 256 and 1024 Hz using different recording systems, depending on the hospital. The iEEG recordings were synchronized with the stimulus events and the patient's behavior in the task by means of pulses on a spare recording channel. To eliminate potential line noise, the recordings were filtered by removing from its Fourier transform the three coefficients centered at 60 and 120 Hz (United States) or centered at 50 and 100 Hz (Europe), followed by the inverse Fourier transform. The recording from each electrode was rereferenced to the average of all electrodes.

Task

These iEEG recordings were obtained while the patients performed in a working memory task (Sternberg, 1966) (see Supplemental Fig. 1). In this task, patients were presented a series of letters (from 1 to 6) at a rate of approximately one letter per second. At the beginning of a trial, first a fixation cross appeared, and then the letters (all consonants) were displayed sequentially on a computer screen. Each letter was on screen for 700 ms, followed by 275–350 ms (uniformly distributed) of blank screen. Patients were instructed to closely attend to each stimulus presentation and to silently hold the identity of each item in memory. The last letter was followed by an additional retention interval of approximately 500 ms, after which a probe letter was presented and the patient had to respond with a key press whether or not it had been presented in the series just before. After the key press, the computer indicated whether the response was correct, and the participant could initiate the next list with a key press.

Because of the limitations of the hospital testing environment, we were unable to measure patients' eye movements during the task. However, we frequently reminded patients to fixate their gaze to minimize unnecessary eye movements.

Weighted phase-locking factors

We measured the strength of the PAC by a weighted phase-locking factor (wPLF) (see Lachaux et al., 1999, for the original definition of the phase-locking factor for the purpose of quantifying phase consistency). This wPLF is a complex-valued association measure of which the magnitude measures the coupling strength and the phase gives the preferred phase angle of the high-frequency bursts in the low-frequency oscillation. The calculation of the wPLF is shown schematically in Fig. 2. The basis of this calculation is a complex-

valued signal, obtained from a convolution of the raw signal with a complex wavelet. With this convolution we estimate the time-varying amplitudes and phases for the different frequency bins that are provided by a wavelet filter bank. The time-varying amplitudes are obtained by the taking the absolute value of the wavelet transform, producing the so-called amplitude envelope. The wavelet transform and the amplitude envelope are mean-centered[1] and normalized.[2] We then take the inner product[3] of these two signals. This results in a complex number of which the magnitude is bounded by 1. Finally, the wPLFs are obtained by averaging the epoch-specific complex inner products over the epochs.

We now describe the calculation of the wPLFs in more detail. The signal recorded at channel i is denoted by x_i. The continuous wavelet transform of x_i is denoted by $\text{wav}(x_i; f)$. The wavelet coefficients are chosen such that this transform provides an estimate of the time-varying amplitudes and phases in the frequency band indexed by f. In our analyses, we used three cycles of a complex sinusoid $\exp(jt)$ ($t = $ time, $j = \sqrt{-1}$) multiplied by a Hanning taper. In principle, we could also have started from analytic signals that are obtained in a different way, for instance, by band-pass filtering followed by the Hilbert transform (Bruns, 2004; Le Van Quyen et al., 2001). The essential point is that we need complex-valued signals that estimate the time-varying amplitudes and phases in a number of frequency bands.

The element-wise absolute value (magnitude) of the wavelet transform, $\text{abs}(\text{wav}(x_i; f))$, is the amplitude envelope. We mean-centered this signal to remove the positive offset that is produced by taking the absolute value of the wavelet transform. Mean-centering is required if one wants to compare PAC across experimental conditions by means of wPLFs. These conditions may differ with respect to the mean amplitude in the wavelet's frequency band, and we do not want the cross-condition differences between the wPLFs to be affected by these amplitude differences. Subsequently, this mean-centered signal was normalized, that is, divided it by its norm. The resulting signal is denoted by $\mathbf{a}_{if}$. The same two operations (mean-centering and normalization) were also applied to the wavelet transform, $\text{wav}(x_i; f)$, and the resulting signal is denoted by $\mathbf{p}_{if}$. The phase angle of the complex-valued signal $\mathbf{p}_{if}$ estimates the phases in x_i with respect to frequency band f.

The basis for the calculation of the wPLF is the inner product of the two signals, $\mathbf{a}_{if}$ and $\mathbf{p}_{i'f'}$. This inner product is denoted by $\langle \mathbf{a}_{if}, \mathbf{p}_{i'f'} \rangle$. The two signals can belong to the same ($i = i'$) or to different channels ($i \neq i'$). Also, they can be obtained using wavelet coefficients of the same frequency ($f \neq f'$) or of different frequencies ($f \neq f'$). Because $\mathbf{p}_{i'f'}$ is normalized, $\langle \mathbf{a}_{if}, \mathbf{p}_{i'f'} \rangle$ gives the explained variance in the mean-centered amplitude envelope $\mathbf{a}_{if}$ by the phase information in the normalized wavelet transform $\mathbf{p}_{i'f'}$. This explained variance is a complex number of which the absolute value is the explained variance and the angle is the preferred phase of the PAC.

The wPLF is obtained by averaging[4] $\langle \mathbf{a}_{if}, \mathbf{p}_{i'f'} \rangle$ over independent epochs:

$$\text{wPLF} = \text{Avg} \langle \mathbf{a}_{if}, \mathbf{p}_{i'f'} \rangle \qquad (1)$$

In our study, the epochs are trials, each corresponding to one item of the Sternberg working memory task. Because the inner products

---

[1] "Mean-centering" is performed by first calculating the mean of the signal (by averaging over the samples) and then subtracting this mean from the signal.

[2] "Normalizing" is performed by first calculating the norm of the signal (the square-root of the inner product of the signal with its conjugate transpose) and then dividing the signal by this norm.

[3] The inner product of two centered and normalized vectors is equivalent to a correlation coefficient. The inner product of two centered *un*normalized vectors is equivalent to a covariance.

[4] As an alternative to averaging over epochs, one can also concatenate the epoch-specific amplitude envelopes and raw wavelet transforms, mean-center and normalize these concatenated vectors, and calculate a single inner product.
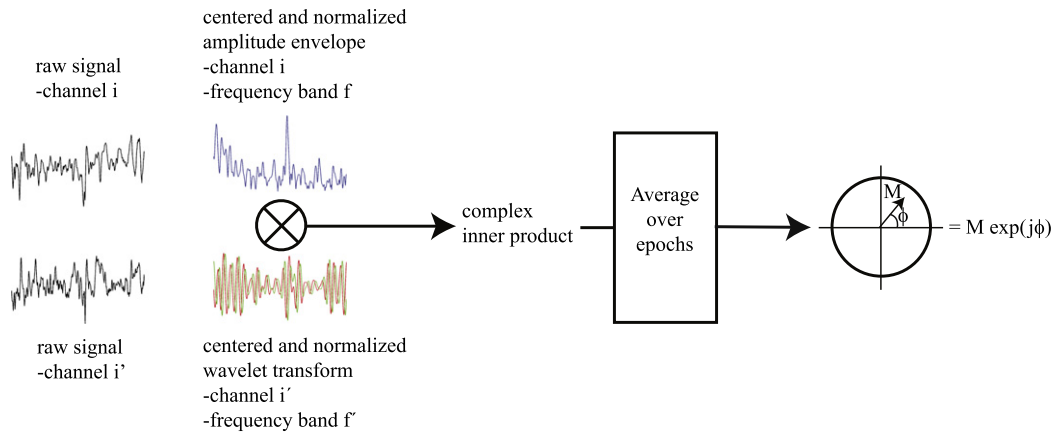
Fig. 2. Schematic of the calculation of the weighted phase-locking factor (wPLF). Raw signals from channels i and i' are convolved with a frequency-indexed wavelet, with indices f and f', producing complex-valued signals. With this convolution we estimate the time-varying amplitudes and the phases for the different frequency bins that are provided by our wavelet filter bank. The wPLF is obtained by taking the average over epochs of the inner products (complex covariances) of an amplitude envelope and a wavelet transform. Prior to calculating the inner product, the amplitude envelopes and the wavelet transform are centered (i.e., their mean is subtracted) and normalized (i.e., dividing the signal by its norm, the square-root of the inner product of the signal with its conjugate transpose). The wPLF is a complex association measure, with absolute value between 0 and 1.

$\langle \mathbf{a}_{if}, \mathbf{p}_{i'f'} \rangle$ are complex, their average over independent epochs can be seen as a weighted phase-locking factor. It is a phase-locking factor because the average depends on the consistency over epochs of the phase angles of the epoch-specific $\langle \mathbf{a}_{if}, \mathbf{p}_{i'f'} \rangle$, and it is weighted because these phase angles are weighted by the magnitude of the $\langle \mathbf{a}_{if}, \mathbf{p}_{i'f'} \rangle$, the square-root of the variance in $\mathbf{a}_{if}$ that is explained by $\mathbf{p}_{i'f'}$.

Because, prior to calculating the inner product, the amplitude envelopes are normalized, the resulting wPLFs will also be called normalized. The maximum magnitude of the normalized wPLFs (square-root of the explained variance) is 1.[5] We chose to normalize the amplitude envelopes because, otherwise, the resulting non-normalized wPLFs would not only reflect the PAC strength but also the power in the particular (channel, frequency)-pair for which the amplitude envelope was calculated. For instance, non-normalized wPLFs reflect the 1/f-dropoff in power with frequency, typical for electrophysiological data. Also, iEEG-channels often show large differences in power, and this is reflected in the non-normalized wPLFs.

Canolty et al. (2006) proposed a measure that is closely related to the non-normalized wPLF. The main difference is that in the measure of Canolty et al. (2006), instead of the normalized wavelet transform $\mathbf{p}_{i'f'}$, a complex phase variable is used that is obtained from $\mathbf{p}_{i'f'}$ by element-wise division by its amplitude abs($\mathbf{p}_{i'f'}$). Canolty et al. (2006) derived their measure as the time average of an analytic complex-valued signal and not as an inner product. However, except for the element-wise division of $\mathbf{p}_{i'f'}$ by abs($\mathbf{p}_{i'f'}$), the two calculations are equivalent.

The precise calculation of the wPLFs depends on a number of parameters of the data sets that are analyzed: the sampling rate, the trial length, and the number of trials. First, the maximum frequency of the wavelet transform is determined by the sampling rate. We wanted every cycle of a wavelet to consist of at least four samples. This set the maximum frequency of the wavelet transform equal to the sampling rate divided by four. We analyzed data sets of four different sampling rates, 256, 400, 512, and 1024 Hz, and therefore the maximum frequencies were 64, 100, 128, or 256 Hz, depending on the data set. Second, the minimum frequency of the wavelet transform is determined by the trial length. In our study, the trials had a length between 1.5 and 6.5 s. The trial length depends on the number list items in the Sternberg working memory task, which ranges from 1 to 4. Because we wanted the minimum frequency to be 1 Hz, prior to

calculating the wavelet transform, we pre- and post-padded the trials with data segments of 2 s. From the wavelet transform, obtained from a convolution with padded trials, we then removed all samples that correspond to that part of the convolution that was obtained with less than 50% of the samples in the non-padded (original) trials. That is, we removed samples for which the overlap between the wavelet and the original trial samples was less than 50%. In this way, we obtain wavelet transforms of the same length as the original trials. Finally, the calculation of the wPLF involves an average over trials (see Eq. (1)). The number of trials differed across patients and ranged from 90 to 336. Trial averages were calculated separately for every patient.

The characterization of the spectral signature of PAC depends on the frequencies for which we estimate the amplitude envelopes and the frequencies for which we estimate the phase. We used the same frequencies for the amplitude envelopes and the phases. To estimate the amplitude envelopes and the phases, we used wavelets that span exactly three cycles. These wavelets were constructed by concatenating three discretely sampled one-cycle complex sinusoids. The time interval between all adjacent samples in the three-cycle wavelet must be equal, and this constrains the possible frequencies, especially at the high end of the spectrum. We attempted to construct a linearly spaced frequency axis between 1 Hz and the maximum frequency (as determined by the sampling rate) with a distance of 1 Hz between adjacent frequencies. However, because of the constraint of an equal interval between adjacent samples, the frequency axis was more narrowly spaced in the low frequency then in the high frequency range (i.c., with a sampling rate of 256 Hz, the first three frequencies are 1 Hz, 2 Hz and 3.0118 Hz, and the last three are 42.6667 Hz, 51.2 Hz, and 64 Hz).

Source characterization

The wPLFs are organized in a four-dimensional array with two spatial and two frequency dimensions: (1) the channels from which the amplitudes were estimated, (2) the channels from which the phases were estimated, (3) the frequency bins of the amplitude estimates, and (4) the frequency bins of the phase estimates. We want to extract the underlying sources from the patterns of PAC in this array. In the following, we show that this is possible using tensor decomposition. This technique is based on the assumption that a source is characterized by two patterns: (1) a real-valued spatial map that specifies how strongly source activity affects the measurements at the level of the sensors, and (2) its frequency spectrum. More

---

[5] This follows from an application of the Cauchy-Schwarz inequality to the normalized vectors a_{if} and $p_{i'f'}$.

specifically, let a_i be the weight of the i-th sensor in the spatial map that characterizes the source, then the frequency spectrum of the source activity measured by this sensor equals a_i times this frequency spectrum. As a consequence, the frequency spectra recorded at different sensors are proportional. This type of source can be produced by a connected network of neurons of which the constituent neurons receive synaptic input with the same oscillatory dynamics.

Not all patterns of neuronal activity can be fully described by a spatial map and a frequency spectrum, and we now give two examples.[6] First, consider a small patch of cortex that shows bursts of high frequency activity which triggers inhibition both locally and in surrounding areas. This inhibition has a longer decay time than the duration of the high frequency bursts. When inhibition wears off, the localized high-frequency burst reoccurs, and the pattern repeats to produce periodic activity. Clearly, the small patch showing high frequency bursts and the surrounding areas have different frequency spectra, and therefore this pattern of neuronal activity will not be considered a single source; for the definition of source used here, all sensors oscillate at the same frequency (but perhaps with different amplitudes).

As a second example, consider coherent distributed neuronal activity that is characterized by a sinusoidal waveform for some part of the source and a sawtooth waveform for the rest. The part with the sawtooth waveform has a frequency spectrum with a different shape than the one in the part with the sinusoidal waveform: the former has relatively more energy in the high frequencies and as a result the two frequency spectra are not proportional. Therefore, this pattern of neuronal activity will not be considered a single source.

Tensor decomposition of weighted phase-locking factors

A source configuration that generates PAC is characterized by two spatial maps and two frequency spectra: (1) the spatial map of the high-frequency phase-coupled bursts, (2) the spatial map of the low-frequency coupling oscillation, (3) the frequency spectrum of the phase-coupled bursts, and (4) the frequency spectrum of the coupling oscillation. Crucially, these maps and spectra can be extracted from the four-dimensional array of wPLFs by means of tensor decomposition (Bro, 1997). This important result follows from (1) the fact that this array of wPLFs can be decomposed as a sum of tensor products, one for every source configuration that generates a pattern of PAC and (2) the fact that this tensor decomposition is unique up to permutation and scaling (see Supplemental Material).

Tensor decomposition is a generalization of singular value decomposition (SVD) to arrays with more than two dimensions. Using SVD, one can express every two-dimensional array as the tensor product of two sets of scaled singular vectors. However, this tensor decomposition is not unique, because the result of the tensor product does not change if the two sets of scaled singular vectors are rotated. Therefore, it does not make sense to interpret these scaled singular vectors in terms of the mechanism that produces the two-dimensional data array. In contrast, with the exception of a few exotic cases, all tensor decompositions of three- and higher-dimensional arrays are unique (Harshman, 1972; Kruskal, 1976, 1977; Leurgans et al., 1993; Sidiropoulos and Bro, 2000). This uniqueness[7] of a tensor decompo-

sition is crucial for its interpretation in terms of the spatial maps and the frequency spectra of the source configuration that produces the sensor-level PAC. In fact, if multiple tensor decompositions would exist for a given four-dimensional array of wPLFs, then one would not know which one of these decompositions would correspond to the spatial maps and the frequency spectra of the true source configuration.

The tensor decomposition of an array of wPLFs is described in detail in the Supplemental Material. In the Results section, we present the main ideas behind the technique by means of an example that shows part of the results for one of the patients in our study.

The uniqueness of the tensor decomposition has been exploited previously in the neuroscience literature: three-dimensional tensor decomposition has been proposed both for the analysis of EEG/MEG and for the analysis of fMRI data (Beckmann and Smith, 2005; Miwakeichi et al., 2004; Mocks, 1988; Morup et al., 2006). We contribute to these methodological developments by proposing a tensor-decomposition that is (1) model-driven (because it can be derived from a few plausible assumptions; see Supplemental Material) and (2) that can deal with phase relations between neuronal signals. Phase relations are at the core of cross-frequency PAC. To identify this coupling, we developed a complex-valued tensor decomposition, complementing the existing real-valued tensor decomposition (see Supplemental Material). The algorithm for this complex-valued tensor decomposition is currently an experimental module in FieldTrip (http://www.ru.nl/neuroimaging/fieldtrip), an open source Matlab toolbox developed at the Donders Institute for Brain, Cognition and Behavior (Nijmegen, the Netherlands). This module will become part of the official Fieldtrip release in the course of 2011.

Data analysis

For every subject, we calculated two arrays of wPLFs: one for the activation period of the Sternberg task, involving encoding and retention of the list items, and one for an equal-length baseline period prior to the presentation of the first list item. These two arrays were analyzed separately as well as jointly. In this joint analysis, all PAC patterns were extracted: baseline-period specific patterns, activation-period specific patterns, and patterns that are observed in both periods (see Supplemental Material). This joint analysis allows us to compare the baseline and the activation period with respect to the amount of variance in the wPLFs that is explained by a particular PAC pattern.

To perform a tensor decomposition, one must know the so-called rank of the array of wPLFs. This rank is the number of components into which the array is decomposed (see Supplemental Material). For every data set, this rank was estimated on the basis of the split-half reliability[8] of the tensor decomposition. For a given data set, we randomly split the trials in two halves, and separately for every half, we calculated the array of wPLFs. We then applied tensor decomposition to both arrays for increasing ranks (beginning at rank 1) and calculated between-half correlations for each of the two spatial maps and the two frequency spectra. The algorithm for least-squares estimation was iterative and started from random starting values.

For every number of components, we calculated correlations between the corresponding spectra in a pair. For a K-component decomposition, this produces four K-by-K matrices of split-half correlations, one for every spectrum. For every rank K, we evaluated whether the two decompositions had matched components with a

---

[6] Both examples were suggested by a reviewer.

[7] There are a two transformations of the tensor decomposition that violate uniqueness in a strict sense, namely permutation and scaling. However, these transformations do not hamper the interpretation of the decomposition in terms of the spatial and frequency spectra of the underlying physiological sources. This is obvious for permutation, which involves a redistribution of spectra over the components of the tensor decomposition (e.g., the four spectra of component 1 become the four spectra of component 2, and vice versa). The scaling transformation involves multiplication of one spectrum by a factor x and another spectrum by the factor $1/x$. It is important to note that this transformation does not affect the shape of the spectra, and therefore the characteristics of the underlying physiological sources that are important for the interpretation are visible in every decomposition (i.e., regardless of the transformation).

[8] Split-half reliability is a method that has its origin in classical test theory (Lord FM, Novick MR. 1968. *Statistical theories of mental test scores*. Reading: Addison-Wesley). It is commonly used to calculate the reliability of a psychological test score.

split-half correlation larger than 0.85 for each of the four spectra. The highest rank for which this was possible, was our rank estimate.

With a critical correlation of 0.85, we never falsely detected PAC patterns in simulated data structures without PAC (data not shown). These simulated data structures were constructed by randomly pairing the amplitude envelopes of one trial with the wavelet transforms of a different trial of the same length. After this random pairing, the wPLFs were calculated as described above.

Quantifying and testing the extent of the spatial spectra

To find evidence for the hypothesis that patterns of PAC are generated by multiple sources, we compared the spatial maps for the phase-coupled bursts with the associated spatial maps for the coupling oscillation. For each of the pairs of spatial maps, we quantified their spatial extent by means of a weighted sum of the inter-electrode distances.

We calculated the inter-electrode distances d_{ij} from the electrode positions in MNI coordinates. Then, to quantify the extent of a spatial map, we first normalized this map (i.e., divided it by its Euclidean norm). The resulting coefficients are denoted by $\mathbf{a} = (a_1, \ldots, a_I)$, in which I denotes the number of electrodes. The larger the coefficient a_i, the more the signal at the corresponding electrode reflects the source that is characterized by this spatial map. We then calculated the following weighted sum of inter-electrode distances[9]:

$$\sum_i^I \sum_j^I |a_i||a_j|d_{ij},$$

in which $|a_i|$ and $|a_j|$ are the absolute values of a_i and a_j. This weighted sum is small if the large coefficients in a spatial map are at a short distance from each other, and large if they are at a long distance.

In this way, we quantified the extents for every pair of spatial maps. We then statistically tested the difference between the members of these pairs by means of a pair-wise t-test. Some patients contributed multiple pairs of spatial maps to this t-test.

Calculating the central frequency of a spectrum

We want to characterize the patterns of PAC by the frequency spectra (see the Results section and the Supplemental Material) of the coupling oscillations and the associated phase-coupled bursts. We summarized every frequency spectrum by its central tendency, which will be called the *central frequency*. The central frequency is calculated as a weighted average of frequencies, with the weights being the coefficients of the frequency spectrum.

Quantifying the consistency over channels of the preferred coupling phases

We quantified the cross-channel consistency of the preferred coupling phases by a weighted phase locking factor, which we will call the cross-*channel* wPLF to distinguish it from the cross-*trials* wPLF with which we quantify the PAC. From the tensor decomposition we obtained a complex-valued spatial map of the phase-coupled bursts of high-frequency activity. This spatial map is denoted by $\mathbf{a} = (a_1, \ldots, a_I)^t$. The magnitudes of these complex coefficients reflect the coupling strength and their phases reflect the preferred phase of the coupling. To quantify the cross-channel

consistency of these preferred phases, we calculate the following wPLF:

$$\frac{\sum_{i=1}^{I} a_i}{\sum_{i=1}^{I} |a_i|}$$

This cross-channel wPLF is a phase-locking factor because the magnitude of the numerator depends on the cross-channel consistency of the phases of the complex coefficients, and it is weighted because it depends on the amplitudes of these complex coefficients. We took the magnitude of the cross-channel wPLF as our quantification of the cross-channel consistency of the preferred coupling phases.

Comparing the activation and the baseline period

We want to compare the activation and the baseline period with respect to the PAC strength of the different patterns. As described before, the squared magnitude of a normalized wPLF can be considered as the proportion of explained variance in the amplitude envelope of some channel by the phases of some other channel. We use the explained variance metric to compare the activation and the baseline period with respect to the PAC strength. In fact, using tensor decomposition, we can calculate the total variance in some array of wPLFs (over all channels and all frequencies) that is explained by a particular PAC pattern (see Supplemental Material). It is also possible to calculate this PAC-pattern-specific total variance separately for the activation and the baseline wPLFs. We do this in a joint tensor decomposition of the activation and the baseline wPLFs, in which we use plug-in estimates of the spatial map of the coupling oscillation and the two frequency spectra obtained from the separate analyses of the activation and the baseline wPLFs. For every PAC pattern identified in the activation and/or the baseline wPLFs, we then calculate the amount of explained variance, separately for the activation and the baseline wPLFs.

We compared the activation and baseline explained variances by means of a paired-samples t-test, in which the pairs are the PAC patterns that were identified in either the activation or the baseline wPLFs, or in both. A disadvantage of this t-test is its inability to detect reliable differences between the activation and the baseline period that cancel each other out, that is, reliable differences that are positive for a subset of PAC patterns and negative for another subset. To test for the existence of such a scenario, we used the random split-half arrays of wPLFs that were also used for determining the rank of the tensor decomposition. We applied the joint tensor decomposition of activation and baseline data to each of the two random split-half arrays. If there are reliable differences between the activation and the baseline period, then they should show up in both analyses. To test this, we calculated the number of PAC patterns for which the difference between the activation and the baseline explained variance had the same sign (both positive or both negative). This number was subsequently tested for significance using a binomial test of the null hypothesis that the probability of a same-sign difference is 0.5.

Results

We did a systematic analysis of the PAC that is present in the iEEG of 26 patients. With this analysis, we want to answer the following four questions: (1) is PAC in a working memory task produced by a single or multiple sources, and (2) what are the frequency bands of the coupling oscillations and the associated phase-coupled bursts, (3) does the coupling oscillation synchronize the phase-coupled bursts, and (4) is PAC involved in working memory operations?

The input of our analysis is a four-dimensional array of weighted phase-locking factors (wPLFs, see Materials and methods). A wPLF is a

---

[9] We also tried several other quantifications of spatial extent, but always obtained the same results. For instance, we also calculated a measure which normalizes the weighted inter-electrode distance by dividing it by the summed unweighted inter-electrode distance. This quantification normalizes for differences across subjects in the physical dimensions of the electrode montage.

complex-valued association measure of which the magnitude measures the coupling strength and the phase gives the preferred phase angle of the high-frequency bursts in the low-frequency oscillation. We calculated this wPLF for every (channel, channel, frequency, frequency)-quadruplet, in which the first channel and the first frequency index the amplitude envelope and the second channel and the second frequency index the time-varying phase. PAC patterns can be described using two spatial maps (one for the phase-coupled bursts and one for the associated coupling oscillation) and two frequency spectra (one for the phase-coupled bursts and one for the associated coupling oscillation) (see Materials and methods). Using tensor decomposition, we extracted the spatial maps and the frequency spectra from the off-diagonal (cross-channel) elements of this four-dimensional array of wPLFs.

Representative tensor decomposition output

We now present the main ideas behind the tensor decomposition by means of the example in Fig. 3, which shows part of the results and part of the array of wPLFs for one of the participants in our study. In panels a–e, we show the spatial maps and the frequency spectra that are produced by the tensor decomposition. In panels f–j, we show three two-dimensional slices in the frequency-by-frequency plane taken from the four-dimensional array of wPLFs for three selected channel pairs. In panels a and b, we show the complex-valued spatial map of the phase-coupled bursts. The magnitude of this map, superimposed on an anatomical MRI (panel a), reflects the coupling strength. The phases of this map, shown in a compass plot (panel b), reflect the preferred phases of the phase-coupled bursts. Note that not all channels have the same preferred phase. However, as will be discussed later in this Results section, the general tendency across all subjects is that the preferred phases are predominantly clustered in one direction. In panel d, we show the frequency spectrum of these phase-coupled bursts, which has a peak at 33 Hz. In panel c, we show the real-valued spatial map of the coupling oscillation, and in panel e we show its frequency spectrum, which has a peak at 9 Hz.

Channels with positive and negative values in the spatial map of the coupling oscillation show this oscillation in antiphase. This aspect of the spatial map reflects the pattern in the wPLFs that is exemplified in the bispectra in panels f–j. All bispectra were obtained from the amplitude envelopes of the channel whose bursts of 33 Hz activity are most strongly modulated by the phase of the coupling oscillation (i.e., the red channel in panel a). The phases were estimated from three different channels: a channel that has a negative value in the spatial map of the coupling oscillation (panels f and g), a channel that has a positive value in this map (panels h and i), and a channel that has a near-zero value (panel j). Panel f, h, and j show the magnitudes of the complex wPLFs, and panels g and i show the phases that correspond to panel f and h, respectively. Because the phases can only be reliably estimated when there is coupling between the high frequency amplitude envelope and the low frequency phases, the phase bispectra in panels g and i are masked by the corresponding magnitude bispectra. The phase bispectrum that corresponds to panel j is omitted because its figure would be completely opaque. Note that the bispectra show two patterns of PAC, one centered at the

pair (9 Hz, 33 Hz), and one centered at the pair (1 Hz, 8 Hz). In panels a–e, we only show the spatial maps and the frequency spectra of the first pattern. The second pattern has different spatial maps and frequency spectra. In the final paragraph of this section, we return to this issue of multiple patterns of PAC in the same data set.

The most important observation with respect to the bispectra in panels f–j is that the magnitude bispectra in panels f and h are very similar (they only differ in strength and not in pattern) whereas their corresponding phase bispectra differ by approximately $\pi = 3.14$. This reflects the fact that, in the first channel, the bursts of 33 Hz activity are locked to the trough of the 9 Hz oscillation (panel g), and in the second channel, they are locked to its peak (panel i). This pattern in the wPLFs is captured by the fact that these two channels have values with opposite signs in the spatial map of the coupling oscillation (panel c).

Note that the extent of the spatial map that characterizes the phase-coupled bursts (the red and green electrodes in panel a) is much smaller than the extent of the spatial map that characterizes the coupling oscillation (the orange, green and blue electrodes in panel c). This was observed in almost all PAC patterns in this pool of participants.

The wPLFs depend on the spatial maps and the frequency spectra via their tensor product. That is, for a given cell in the four-dimensional array of wPLFs, (1) the contribution of a particular PAC pattern is obtained as the product of the corresponding coefficients in the two maps and the two spectra, and (2) the contributions of different PAC patterns add up.

In Fig. 3, we show the spectra of only a single pattern of PAC. However, an array of wPLFs may very well contain multiple patterns of PAC, each characterized by its own set of spatial maps and frequency spectra. In fact, it is clear from the bispectra that there is also a PAC pattern centered at the pair (1 Hz, 8 Hz). Mathematically, this translated into the fact that the rank of the array of wPLFs is larger than 1. In Fig. 3, this is indicated by the ellipsis on the right-hand side of the equation.

Existence of reliable phase-amplitude coupling patterns

In the analysis of the activation period wPLFs, 36 reliable PAC patterns were identified: two subjects had four reliable PAC patterns, eight had two, 12 had one, and four had none. In the analysis of the baseline period wPLFs, 17 reliable PAC patterns were identified: four subjects had two reliable PAC patterns, nine had one, and 13 had none. Reliability was defined in terms of the split-half correlation between two independent estimates of the spatial and the frequency spectra produced by the tensor decomposition. All identified PAC patterns had reliabilities much larger than what can be expected under the hypothesis of a random PAC (see Materials and methods). A representative selection of reliable PAC patterns is shown in Supplemental Fig. 3.

The existence of reliable PAC patterns shows that there is spatial and spectral structure in the array of wPLFs. Because we analyzed the wPLFs that were obtained from pairs of different channels, this structure must result from physiological activity that is measured at multiple sites. From this observation alone, we cannot conclude that

Fig. 3. Illustration of a tensor decomposition of the four-dimensional array of weighted phase-locking factors (wPLFs). The two spatial maps and the two frequency spectra (see text) are each denoted by a different color (red, yellow, green, and blue) and a different index (i, i', f, f'). The same colors are used both for the boundaries of the panels and the symbols in the formula for the wPLF. In panels a and b, with red and index i, we show the complex-valued spatial map of the high-frequency bursts that are coupled to a common low-frequency oscillation (the coupling oscillation). In panel a, we show the magnitude (absolute value) of this complex-valued spatial map (one colored circle per channel), which expresses the strength of the coupling. In panel b we show the phases of the coupling oscillation to which the high-frequency bursts are locked (one arrow per channel). In panel c, with yellow and index i', we show the spatial map of the coupling oscillation (one colored circle per channel). The more a coefficient $b_{i'}$ deviates from zero, the more this channel is affected by the coupling oscillation. In panel d, with green and index f, we show the frequency spectrum of the phase-coupled bursts (shown on a logarithmic scale). In panel e, with blue and index f', we show the frequency spectrum of the coupling oscillation. The spectra shown in panels a, b, c, d and e are all in arbitrary units (a.u.). This is because the spectra are produced by a tensor decomposition which involves an arbitrary multiplicative scaling (see Supplemental Material). In panels f, h, and j, we show the magnitudes of the complex wPLFs for three selected channel pairs (see text). By means of arrows, we connect the channels in panels a and c for which these wPLFs were calculated, with the corresponding x-axes (showing the frequency of the coupling oscillation), respectively, y-axes (showing the frequency of the phase-coupled bursts), in panels f, h, and j. In panels g and i, we show the phases of the complex wPLFs that correspond to panels f and h, respectively.
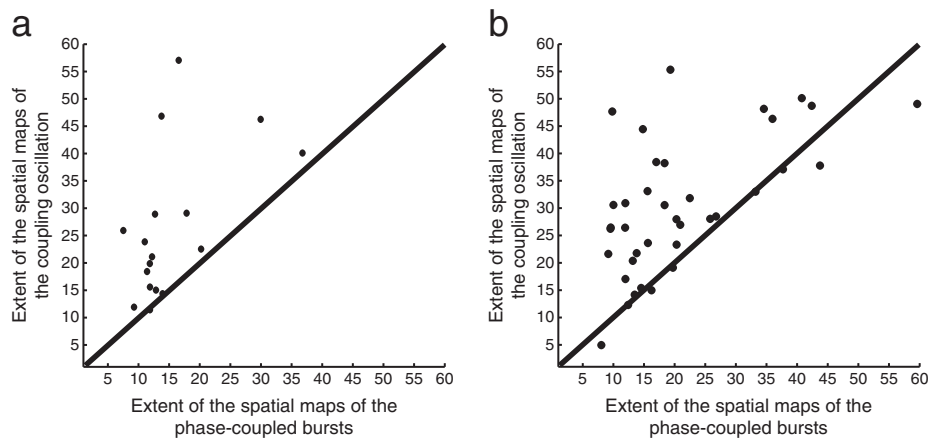
$$\text{wPLF}_{i\,i'\,f\,f'} = a_i\,b_{i'}\,c_f\,d_{f'} + \ldots$$
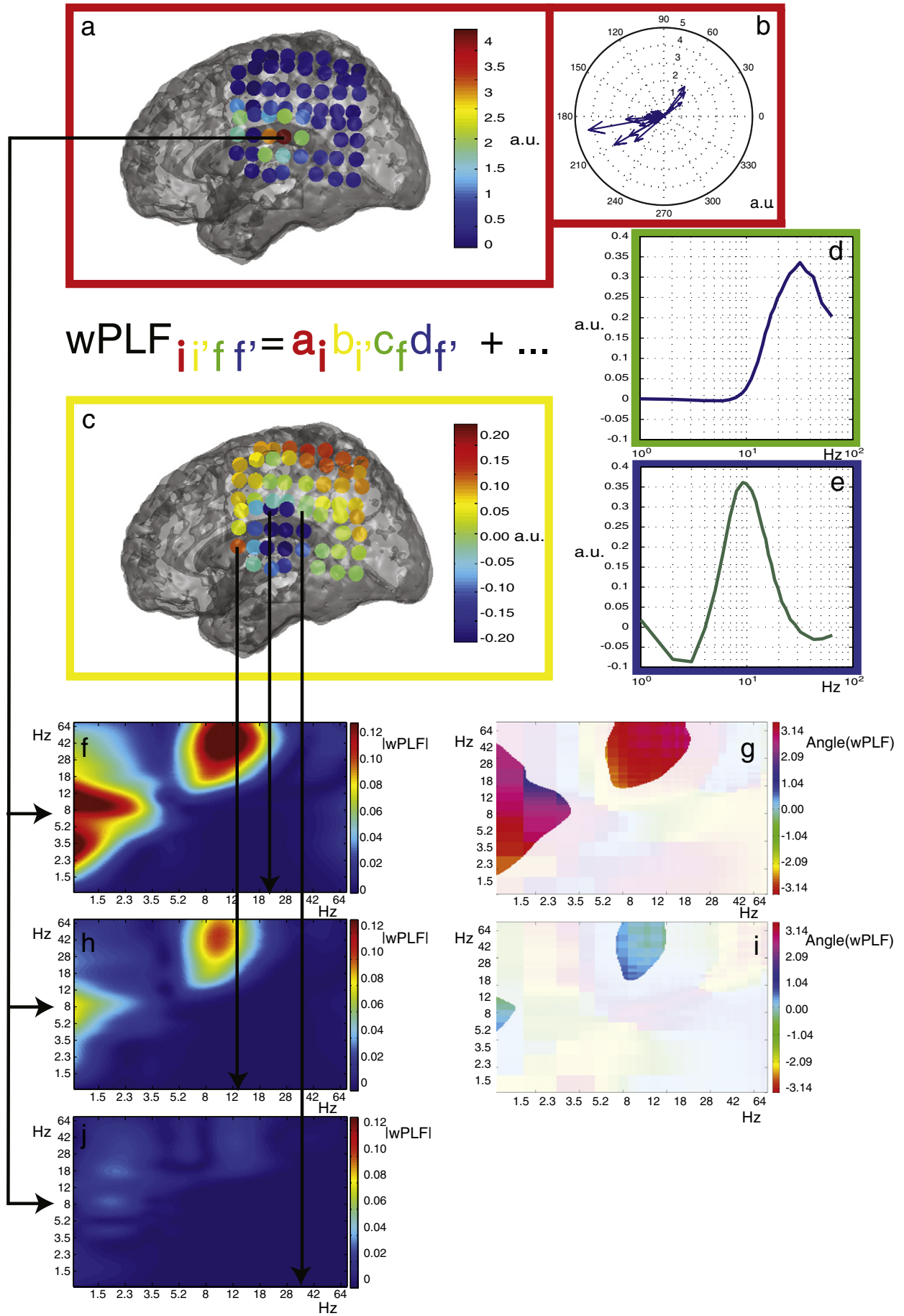
Fig. 4. Spatial maps of the phase-coupled bursts are smaller than the spatial maps of the associated coupling oscillation. Both panels show scatter plots of the extent of the spatial maps of the phase-coupled bursts (horizontal axis) against the extent of the corresponding spatial maps of the coupling oscillation (vertical axis). Panels a and b show the scatter plots for, respectively, the baseline and the activation period. Panels a and b show the scatter plots for, respectively, the baseline and the activation period. In both periods, for most of the PAC patterns, the extent of the spatial map of the phase-coupled bursts is substantially smaller than the extent of the spatial map of the associated coupling oscillation.

multiple sources are involved in the PAC. In fact, a single source that produces a rhythmic signal with a sharp-edged waveform will result in a significant cross-channel PAC, at least if it is measured at multiple sites. However, if there is only a single source active, then the spatial maps of the coupling oscillation and the phase-coupled bursts will be identical.

Comparison of the extent of the two spatial maps

To find evidence for the hypothesis that PAC patterns are generated by multiple sources, we compared the spatial maps for the phase-coupled bursts with the associated spatial maps for the coupling oscillation. For each of the pairs of spatial maps, we quantified their extent by means of a weighted sum of the inter-electrode distances (see Materials and methods). In Fig. 4, we show scatter plots of the extent of the spatial spectra of the phase-coupled bursts (horizontal axis) against the extent of the corresponding spatial spectra of the coupling oscillation (vertical axis). For the vast majority of the pairs, the extent of the spatial map of the phase-coupled bursts is substantially smaller than the extent of the spatial map of the coupling oscillation. This holds both for the activation (Fig. 4b, $t(35) = -6.194$, $p < 0.001$) and the baseline period (Fig. 4a, $t(16) = -4.1027$, $p < 0.001$). This finding cannot be produced by a single source.

Analysis of the within-channel wPLFs

Until now, we have reported on the results of a tensor decomposition of the off-diagonal (cross-channel) elements of the four-dimensional arrays of wPLFs. Thus, we excluded the diagonal (within-channel) elements, which are obtained from single channel data that are filtered twice. However, within-channel PAC is what has been investigated in several previous studies (Canolty et al., 2006; Mormann et al., 2005). Therefore, it is of interest to ask whether the within-channel wPLFs contain the same information as the cross-channel wPLFs. We will show that this is not the case.

In Fig. 5, we give a schematic representation of a two-dimensional slice from the four-dimensional array of wPLFs. The group of yellow entries is produced by bursts of high-frequency activity that are measured by three channels and that are phase-coupled to an oscillation that is measured by eight channels. This pattern of PAC produces significant within-channel as well as cross-channel wPLFs. In contrast, the group of red entries is produced by PAC that is only observed in the within-channel wPLFs. This PAC cannot be produced by a common coupling oscillation that is measured by multiple

channels, because this would have resulted in significant cross-channel wPLFs. However, it can be produced by multiple local coupling oscillations that are only measured by the same channel that also measures the associated phase-coupled bursts. Clearly, such a local PAC cannot play a role in the coordination of neuronal activity over distributed areas (i.e., an area that is covered by more than one electrode). Moreover, and crucial for this paper, it cannot be excluded that these significant within-channels wPLFs are produced by local sources that produce sharp-edged waveforms. In contrast, the yellow group of significant cross-channel wPLFs can only be produced by multiple sources. This is because the extent of this pattern is different for the two spatial dimensions.

The two patterns of PAC will show up differently in the tensor decomposition of the cross-channel and the within-channel wPLFs (see Fig. 5). Remember that the within-channel wPLFs are on the main diagonal of the array. In the analysis of the cross-channel wPLFs, we will only identify patterns of PAC that involve a common coupling oscillation, such as the pattern that produces the yellow group of channel pairs. In the analysis of the within-channel wPLFs, we will also identify the PAC that is produced by multiple local coupling oscillations, such as the pattern that produces the red group of channel pairs. Note that the spatial maps of the coupling oscillation and the associated phase-coupled bursts that describe the structure in the within-channel wPLFs have exactly the same spatial extent (see Fig. 5). This also holds for PAC patterns that are produced by a spatially distributed coupling oscillation, as is clear from the within-channel spatial maps for the yellow group of channel pairs. Thus, the spatial extent of these PAC patterns is incorrectly characterized by the within-channel wPLFs. This is why, to characterize the spatial extent of the PAC patterns, we analyzed the cross-channel wPLFs.

For comparison with our analysis of the four-dimensional array of cross-channel wPLFs, we also applied tensor decomposition to the three-dimensional array of within-channel wPLFs (channels-by-frequencies-by-frequencies). Contrary to the tensor decomposition of the four-dimensional array of cross-channel wPLFs, for every pattern of PAC, we now extract only a single spatial map. This single spatial map corresponds to the element-wise product of the two spatial maps for the cross-channel wPLFs. That is, if a_i and b_i are the loadings for the i-th channel in a spatial map for, respectively, the phase-coupled bursts and the associated coupling oscillation, as obtained from the analysis of the cross-channel wPLFs, then the corresponding loading for the within-channel wPLF analysis is $a_i \times b_i$. Of course, this only holds if the corresponding spatial maps are indeed extracted in the tensor decompositions of both the within- and the cross-channel wPLFs.
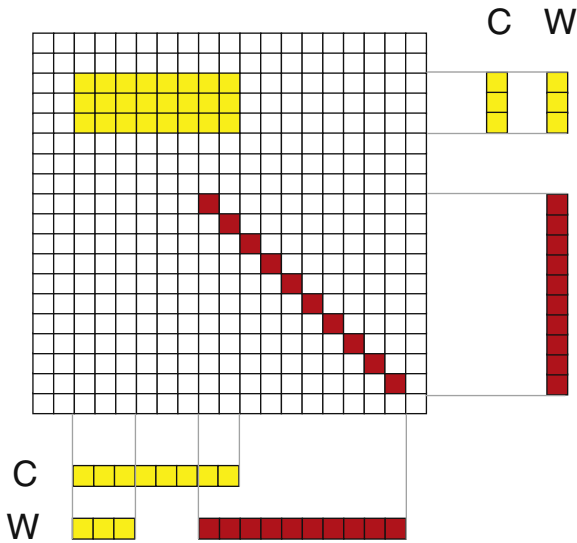
Fig. 5. Differences between cross-channel and within-channel wPLFs with respect to the PAC patterns that they can identify. The two-dimensional array represents a slice that was taken from the four-dimensional array of wPLFs. This slice was taken for a particular pair of frequencies for the amplitude envelopes and the phases. The rows of this slice correspond to the channels for which the amplitude envelopes were calculated, and the columns to the channels for which the phases were calculated. The colored cells indicate significant wPLFs. The spatial maps that characterize the PAC patterns are shown to the right and below the two-dimensional slice. The spatial maps of the phase-coupled bursts and the associated coupling oscillation, as obtained from the tensor decomposition of the cross-channel wPLFs, are shown under, respectively, to the right of the letters B. The single spatial map obtained from the tensor decomposition of the within-channel wPLFs is shown under and to the right of the letters W.

Using the same split-half reliability criterion, we found much more reliable PAC patterns in the tensor decomposition of the within-channel wPLFs than in the tensor decomposition of the cross-channel wPLFs. In the analysis of the activation period within-channel wPLFs, we extracted 105 PAC patterns, as compared to 36 in the analysis of the corresponding cross-channel wPLFs (paired-samples t-test over patients, $t(25) = 9.015$, $p<0.001$). And in the analysis of the baseline period within-channel wPLFs, we extracted 35 PAC patterns, as compared to 17 in the analysis of the corresponding cross-channel wPLFs (paired-samples t-test over patients, $t(25) = 3.9931$, $p<0.001$).

The PAC patterns extracted from the within-channel wPLFs are not only more numerous, they are also more widespread. We calculated the spatial extent of the PAC patterns using the same index that was also used for comparing the spatial extent of the phase-coupled bursts with the spatial extent of the corresponding coupling oscillations (the weighted sum of the inter-electrode distances; see Materials and methods). For the PAC patterns that were extracted from the cross-channel wPLFs, we calculated the element-wise product of the two spatial maps, and compared the extents of these product spatial maps to the extents of the single spatial maps that were extracted from the within-channel wPLFs. Per subject, we calculated the average extent (over the PAC patterns of this subject) for the two corresponding types of spatial maps, one extracted from the cross-channel wPLFs (the product spatial map) and the other from the within-channel wPLFs. In Fig. 6, we show scatter plots of these average spatial extents. For all subjects, the average extent of the product spatial maps extracted from the cross-channel wPLFs is smaller than the one extracted from the within-channel wPLFs. This holds both for the activation (Fig. 6b, $t(22) = -7.9085$, $p<0.001$) and the baseline period (Fig. 6a, $t(9) = -4.7793$, $p<0.001$). The widespread PAC patterns in the within-channel wPLFs are in line with the observation by Canolty et al. (2006) that 84.3% of their electrodes showed significant theta/gamma coupling.

These findings are in line with our theoretical analysis of the difference between the tensor decompositions of the within- and cross-channel wPLFs. In fact, our findings are consistent with the existence of multiple local coupling oscillations, which are only extracted in the tensor decomposition of the within-channel wPLFs. Of course, we cannot rule out that this within-channel PAC is produced by local (channel-specific) sharp-edged waveforms. Further, the more widespread PAC patterns in the within- as compared with the cross-channel wPLFs are most likely produced by local sources with the same bispectral structure (same frequency spectra for the coupling oscillation and the phase-coupled bursts). In fact, if these PAC patterns were produced by spatially distributed sources, then they would also have been observed in the cross-channel wPLFs.

Spectral content of the oscillations

In Fig. 7, we summarize the spectral content of the phase-coupled bursts and the associated coupling oscillations by their central frequencies. The central frequency of the phase-coupled bursts is always larger than the one for the associated coupling oscillations. It is
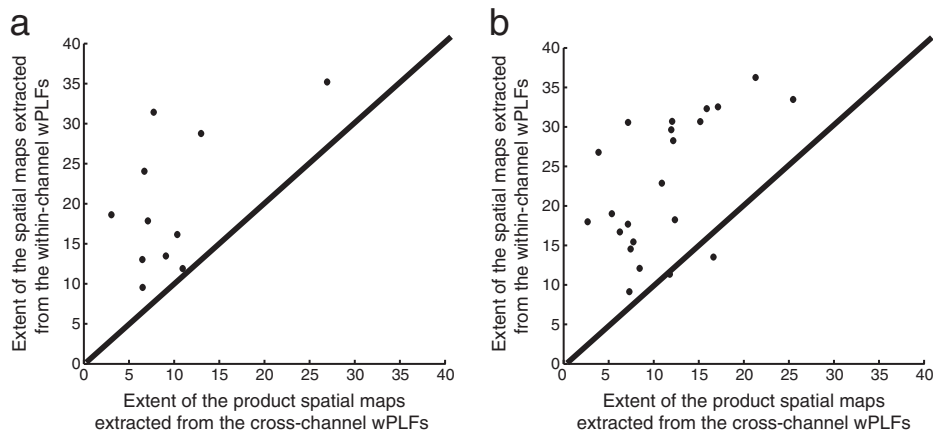

Fig. 6. PAC patterns extracted from the cross-channel wPLFs are smaller than PAC patterns extracted from the within-channel wPLFs. Both panels show scatter plots of the average extent (with averaging over the PAC patterns within a subject) of the product spatial maps extracted from the cross-channel wPLFs (horizontal axis) against the average extent of the spatial maps extracted from the within-channel wPLFs (vertical axis). Panels a and b show the scatter plots for, respectively, the baseline and the activation period. In both periods, for most subjects, the average extent of the product spatial maps extracted from the cross-channel wPLFs is substantially smaller than the average extent of the spatial maps extracted from the within-channel wPLFs. Because there are more subjects with reliable PAC patterns in the activation than in the baseline period, there are also more dots in the scatter plot for the activation than in the one for the baseline period.
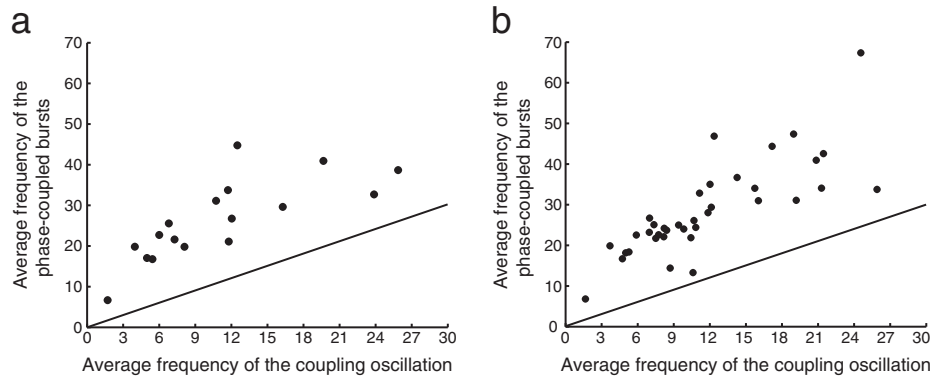
Fig. 7. Spectral signature of the PAC patterns. Panels a and b show the results for, respectively, the baseline and the activation period. Both panels show a scatter plot of the central frequencies of the phase-coupled bursts (horizontal axis) against the central frequencies of the coupling oscillations (vertical axis). The central frequency of the phase-coupled bursts is always smaller than the one for the associated coupling oscillation. For all PAC patterns above the thick black line, the central frequency for the phase-coupled bursts is larger than the central frequency for the associated coupling oscillation. There is not a dominant frequency, neither for the phase-coupled bursts, nor for the associated coupling frequencies.

important to see that there is not a dominant frequency, neither for the coupling oscillations nor for the phase-coupled burst: phase-coupled bursts are in the range 7–70 Hz and coupling oscillations are in the range 2–25 Hz.

Consistency of the preferred coupling phases

A straightforward way to achieve spatio-temporal coordination of neuronal activity is by spatially distributed bursts of high-frequency activity occurring at the same time. Phase-amplitude coupling could be the vehicle via which this coordination is realized, namely if the bursts all occur at the same phase of the coupling oscillation. This can be investigated using the tensor decomposition. In fact, the tensor decomposition allows that the bursts of high-frequency activity in the different channels have a different preferred phase in the coupling oscillation. This is because the spatial spectrum of the phase-coupled bursts is complex-valued. We examined the consistency across the

channels of these preferred coupling phases (see Materials and methods) and found that the majority of the PAC patterns exhibits a strong consistency (Fig. 8). Thus, in the majority of the PAC patterns, the phase-coupled bursts of high-frequency activity are synchronized across brain areas.

Comparison of the baseline and the activation period

PAC has been proposed as the cornerstone of a model for temporal segmentation and integration of items that are kept in working memory (Lisman and Idiart, 1995). This model predicts that theta-gamma PAC is stronger during periods that involve working memory operations than during periods that do not. Inspired by this prediction, we tested whether patterns of PAC are differentially involved in epochs that differ with respect to these working memory operations. In particular, we jointly analyzed the wPLFs of the baseline and the activation period of the Sternberg task. In this joint analysis,
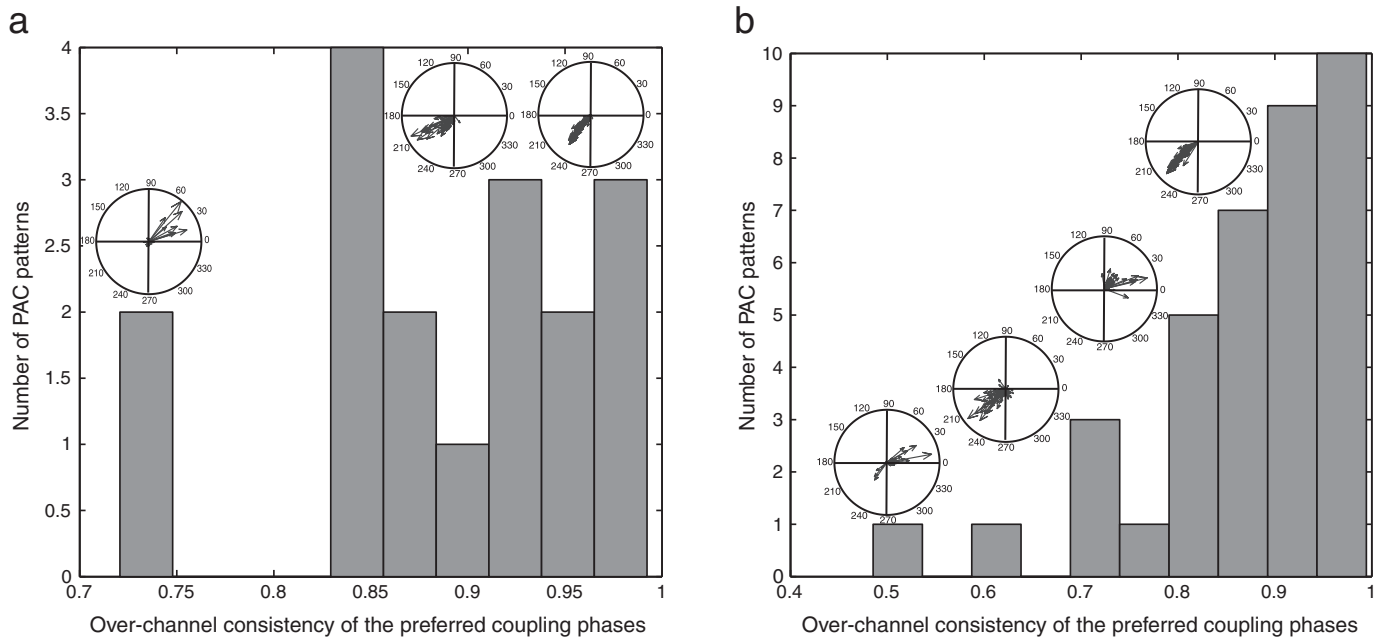

Fig. 8. Consistency over the channels of the preferred coupling phases. Panels a and b show the results for, respectively, the baseline and the activation period. Both panels show a histogram of the absolute values of a cross-channel weighted phase locking factor that quantifies the over-channel consistency of the preferred coupling phases. Next to the histograms, there are example compass plots that illustrate different values of this consistency measure. Both in the baseline and the activation period, the majority of the PAC patterns exhibits a very strong consistency.
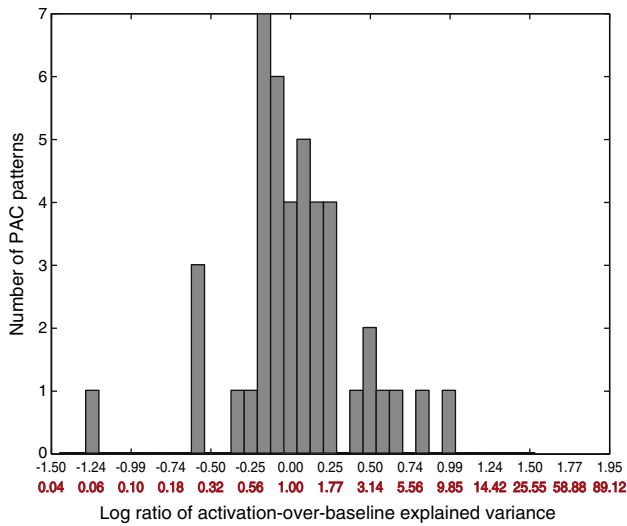
Fig. 9. Histogram of the log ratios of the activation over the baseline explained variances in the phase-coupled bursts. The log ratios are printed black and their corresponding ratios are printed red.

all PAC patterns were extracted: baseline-period specific patterns, activation-period specific patterns, and patterns that are observed in both periods (see Materials and methods).

To quantify the differential involvement of the PAC patterns in the baseline and the activation period, we calculated the variance in the high-frequency amplitude envelopes that is explained by the coupling oscillation, separately for these two periods, and then calculated the difference between the logarithms of these two variances, which is equivalent to calculating their log ratio. The histogram of these log ratios is approximately centered at zero (see Fig. 9), which indicates that working memory operations do not uniformly shift the PAC strengths in either direction (paired-samples t-test of the log variances, $t(42) = -0.4935$, $p = 0.6242$). We arrived at the same conclusion when the non-logarithmically transformed variances were contrasted ($t(42) = 0.6130$, $p = 0.5432$).

The absence of a difference between the average log variance (over PAC patterns) between the activation and the baseline variance does not rule out the possibility that some subset of PAC sources exhibits a stronger coupling in the activation than in the baseline period, whereas the reverse holds for another subset. Positive and negative differences between the activation and the baseline period may compensate for each other in the calculation of the average difference. In fact, this is what happened, and we showed it by separately analyzing two random split-half arrays of wPLFs and evaluating the consistency of the output. The consistency between the two random split-half analyses can be visualized in the scatter plot of the variance log ratios for the two random split-halves (see Fig. 10). The consistency was quantified by means of a binomial test of the number of PAC patterns that have a same-sign variance log ratio between the activation and the baseline period (32 PAC patterns with consistent signs out of 43, $p = 0.0003$). Thus, working memory operations affect the PAC strengths in an heterogeneous way: for some PAC patterns, the strength increases during working memory operations, whereas for others it decreases.

We hoped to increase our understanding of the relation between PAC and working memory by attempting to identify anatomical clusters that show PAC increases and others that show PAC decreases. We selected five components of which the strength reliably decreased by at least 50%, going from baseline to activation, and seven components of which the strength reliably increased by at least 50%. Separately for each of the two sets of components, we plotted the electrodes that exhibit a strong modulation of the coupling strength of the phase-coupled bursts that are measured at these electrodes (see Fig. 11). Because of the low

number of components, and the large heterogeneity across subjects in the electrode layout, one should be careful in interpreting these results. This being said, it seems that PAC decreases (baseline > activation) are predominantly observed over the right temporal lobe, but there also decreases over a few left frontal and left temporal areas. PAC increases (activation > baseline) are predominantly observed over the right temporal and the right parietal lobe, but there are also increases over a few left parietal, left temporal, and right frontal areas.

Discussion

We investigated cross-frequency PAC by identifying structural patterns in four-dimensional arrays of wPLFs that were obtained from iEEG recordings from 26 patients. From the off-diagonal elements of these arrays, we identified 36 reliable patterns in the activation period and 17 in the baseline. This did not require an exhaustive search of the four-dimensional arrays of wPLFs. Instead, the patterns were identified automatically and objectively by means of a tensor decomposition.

It is important to note that the wPLF is not a measure of the spectral content of a single channel, but instead is a spectral association measure: it will deviate from zero if the spectral content of one channel (i.e., its amplitude envelope at a particular frequency) is associated in a particular way with the spectral content of another channel (i.e., its phase at a particular frequency). As a consequence, one cannot expect the same oscillations to show up that were previously identified in the same dataset on the basis of their spectral content, namely oscillations in the theta and the gamma band (Howard et al., 2003; Raghavachari et al., 2001, 2006; Rizzuto et al., 2003; Sederberg et al., 2003; van Vugt et al., 2010, 2009). In our analysis, we only identified those oscillations that are involved in patterns of cross-channel PAC.

We extracted the spatial maps and the frequency spectra that characterize patterns of cross-frequency PAC. We found that the spatial maps of the coupling oscillations are much wider than those of the corresponding phase-coupled bursts (Fig. 4). Every coupling oscillation represents a spatially distributed pattern of phase-consistent oscillatory activity. On a subset of the areas that show this spatially distributed activity, we observe phase-coupled bursts of high-frequency activity.
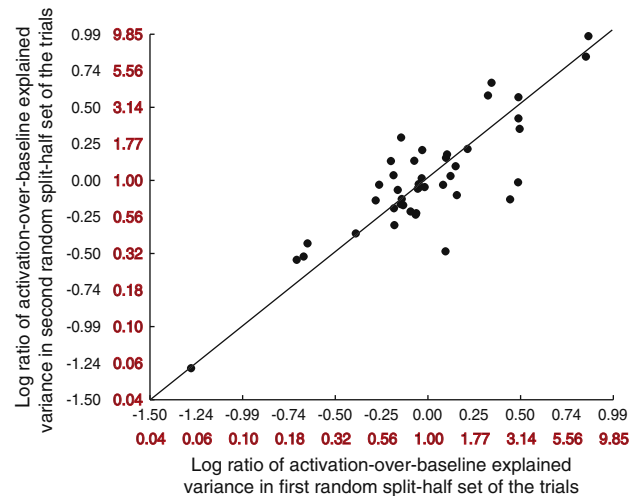

Fig. 10. Reliable differences in PAC strength between the activation and the baseline period. Scatter plot of the log ratios of the activation-over-baseline explained variance calculated separately for two random split-halves of the trials. The log ratios are printed black and their corresponding ratios are printed red. There is a positive correlation between the log ratios in the two random split-halves, and this shows that there are reliable differences between the activation and the baseline period. The scatter plot is centered at 0 and, together with the positive correlation, this shows that there are both positive and negative reliable differences between the activation and the baseline period.

Baseline > Activation
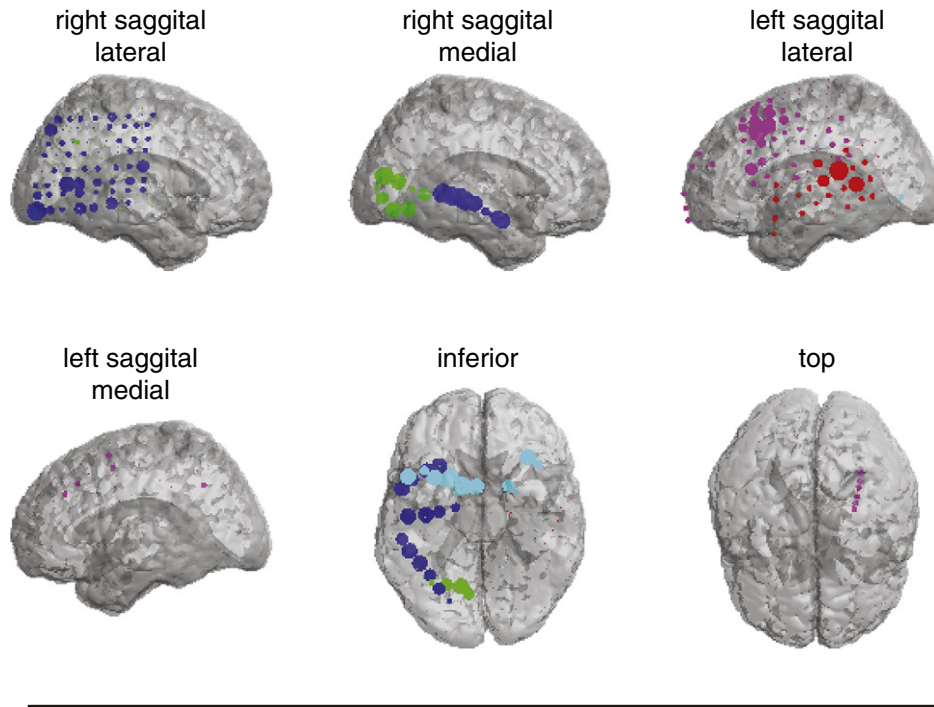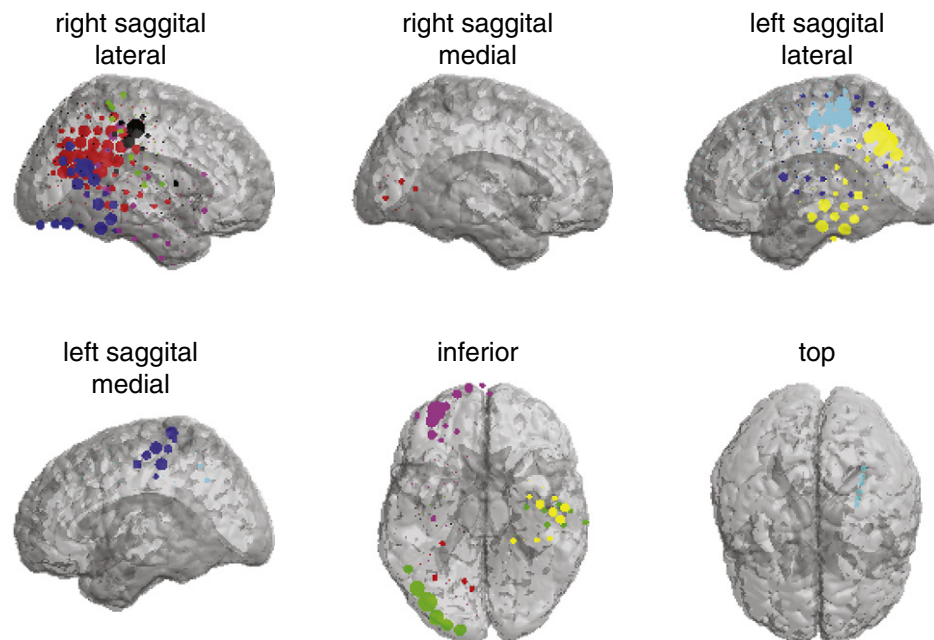

Activation > Baseline

Fig. 11. Localization of components showing a reliable modulation in PAC strength between the activation and the baseline period. The upper panel shows the location of the components with a PAC strength that decreases from the baseline to the activation period. Every component is denoted by a different color. Electrodes are denoted by disks with a diameter proportional to the magnitude of their loadings in the spatial map of the high-frequency bursts. PAC decreases are predominantly observed over the right temporal lobe, but there also decreases over a few left frontal and left temporal areas. The lower panel shows the location of the components with a PAC strength that increases from the baseline to the activation period. PAC increases are predominantly observed over the right temporal and the right parietal lobe, but there are also increases over a few left parietal, left temporal, and right frontal areas.

From the difference in the spatial extent of the coupling oscillations and the corresponding phase-coupled bursts, we conclude that there are patterns of cross-frequency PAC that involve multiple sources.

It is important to note that the tensor decomposition in no way constrains the spatial maps of the coupling oscillations to be wider than those of the corresponding phase-coupled bursts. In fact, if the relation were reversed (less extended spatial maps for the coupling oscillations than for the phase-coupled bursts), the method would also have revealed it, as is clear from simulation studies (data not shown).

The more widespread spatial spectrum of the coupling oscillation is in line with previous studies showing that slow oscillations are generally more widespread (spatially coherent) than fast oscillations. This has been shown using extracranial EEG (von Stein and Sarnthein, 2000), intracranial EEG (Crone et al., 1998a,b), extracellular recordings in monkeys (von Stein et al., 2000), and intracellular recordings in cats (Destexhe et al., 1999). Especially the latter study is convincing, because it is based on signals that are not contaminated by volume conduction. Destexhe et al. (1999) show that oscillations in the 0.1–4 Hz range, which are observed during slow-wave sleep and under anaesthesia, are much more widespread than fast oscillations in the 15–75 Hz range, which are observed during wakefulness and REM sleep.

Our conclusion about the different spatial extents of the coupling oscillations and the associated phase-coupled bursts crucially depends on the information in the cross-channel wPLFs. In fact, from the within-channel wPLFs one can only estimate a single spatial map. Nevertheless, the tensor decomposition of the within-channel wPLFs shows an interesting pattern (more and more widespread PAC patterns than in the tensor decomposition of the cross-channel wPLFs) that may be produced by multiple *local* PAC sources with the same bispectral structure. However, it cannot be ruled out that this pattern is produced by local sharp-edged waveforms.

Published iEEG studies on PAC (Canolty et al., 2006; Mormann et al., 2005) have reported coupling between bursts of gamma activity (>30 Hz) and the phase of a coupling oscillation in the theta band (4–7 Hz). In our study, we did not observe a dominant frequency, neither for the coupling oscillations nor for the phase-coupled bursts: coupling oscillations are in the range 2–25 Hz and phase-coupled bursts are in the range 7–70 Hz. One possible reason for this discrepancy is that coupling oscillations in the theta band may be associated with high-frequency bursts in a range that falls outside the frequency range of our wavelet filter bank. Our analyses are dominated (in 16 out 26 patients) by data sets with a sampling rate of 256 Hz, which is low compared to other studies. For these data sets, the maximum wavelet frequency was 64 Hz (see Materials and methods). However, neither in these data sets, nor in the ones with a higher maximum wavelet frequency (100, 128 and 256 Hz), we observed patterns of PAC in which the coupling strength increased or asymptoted with increasing frequency, as was observed by Canolty et al. (2006). It is thus unlikely that the sampling rate explains the fact that we observed only a small number of coupling oscillations in the theta band. Instead, our results show that PAC is not restricted to the theta-gamma frequency pair. PAC may be a general phenomenon, produced by a particular network architecture in a way that is largely independent of the membrane time constants that characterize the different neuron types participating in this network.

Using the phase information in the spatial maps of the phase-coupled bursts, we showed that, in the majority of the PAC patterns, these bursts are synchronized across brain areas (Fig. 8). This observation is in line with the hypothesis that PAC plays a role in the spatiotemporal coordination of neuronal activity. Importantly, this synchronization is between amplitude envelopes, and not necessarily between the oscillations of which the amplitudes were calculated.

Inspired by the Lisman and Idiart (1995) model, we investigated whether PAC plays a role in the working memory operations encoding and retention. From this investigation, we can conclude that working memory operations do not uniformly shift the PAC strengths in either direction (stronger or weaker than during the baseline period). Instead, working memory operations affect the PAC strengths in a heterogeneous way: in some PAC patterns, the strength increases during working memory operations, whereas in others it decreases. Especially the right temporal lobe appears to be involved in WM-induced modulations of PAC.

Our conclusion about the number of sources involved in PAC depends on our definition of a source. We defined a source in terms of two patterns: (1) a spatial map that specifies how strongly source activity affects the measurements at the sensor level, and (2) its frequency spectrum. We showed that, with this source definition, the array of PAC-measures (wPLFs) can be written as a tensor product of two spatial maps (one complex- and one real-valued) and two frequency spectra (both real-valued), which is exactly the structure that is extracted by our tensor decomposition (see Supplemental Methods). However, we cannot exclude PAC-generating source configurations that cannot be characterized in this way. In fact, we have argued that PAC-patterns may also be generated by a source configuration that would be considered a single source when viewed from the perspective of the mechanism that generates the physiological signal. This confronts us with the problem that sources can be defined both in terms of their formal characteristics (i.e., in terms of a spatial map and a frequency spectrum) and in terms of the neuronal network that generates the physiological signal. The difference between the two definitions is most clear if the physiological mechanism consist of multiple components, such as networks of inhibitory neurons that are connected to one or multiple classes of principal neurons, each with its own network topology. This whole multi-component network may be considered as a single source, but also as multiple sources, each one corresponding to one component. Importantly, if these components differ with respect to their spatial maps and frequency spectra, then they can be extracted by means of tensor decomposition. This shows there may be a need for a linking of the set of extracted source configurations on the basis of the neuronal interactions that may have produced them.

In conclusion, we have shown that PAC is a spatially distributed phenomenon in which the low- and the high-frequency oscillations are characterized by different spatial maps. Second, in the majority of the PAC patterns, phase-coupled bursts of high-frequency activity are synchronized across brain areas. Third and last, working memory operations affect the PAC strength in a heterogeneous way: in some PAC patterns, working memory operations increase their strength, whereas in others they decrease it.

Supplementary materials related to this article can be found online at doi:10.1016/j.neuroimage.2010.09.029.

Acknowledgements

References

Beckmann, C.F., Smith, S.M., 2005. Tensorial extensions of independent component analysis for multisubject FMRI analysis. NeuroImage 25, 294–311.

Bro, R., 1997. PARAFAC. Tutorial and applications. Chemom. Intell. Lab. Syst. 38, 149–171.

Bruns, A., 2004. Fourier-, Hilbert- and wavelet-based signal analysis: are they really different approaches? J. Neurosci. Methods 137, 321–332.

Bruns, A., Eckhorn, R., 2004. Task-related coupling from high- to low-frequency signals among visual cortical areas in human subdural recordings. Int. J. Psychophysiol. 51, 97–116.

Buzsaki, G., Draguhn, A., 2004. Neuronal oscillations in cortical networks. Science 304, 1926–1929.

Canolty, R.T., Edwards, E., Dalal, S.S., Soltani, M., Nagarajan, S.S., et al., 2006. High gamma power is phase-locked to theta oscillations in human neocortex. Science 313, 1626–1628.

Chrobak, J.J., Lorincz, A., Buzsaki, G., 2000. Physiological patterns in the hippocampo-entorhinal cortex system. Hippocampus 10, 457–465.

Crone, N.E., Miglioretti, D.L., Gordon, B., Lesser, R.P., 1998a. Functional mapping of human sensorimotor cortex with electrocorticographic spectral analysis—II. Event-related synchronization in the gamma band. Brain 121, 2301–2315.

Crone, N.E., Miglioretti, D.L., Gordon, B., Sieracki, J.M., Wilson, M.T., et al., 1998b. Functional mapping of human sensorimotor cortex with electrocorticographic spectral analysis—I. Alpha and beta event-related desynchronization. Brain 121, 2271–2299.

Destexhe, A., Contreras, D., Steriade, M., 1999. Spatiotemporal analysis of local field potentials and unit discharges in cat cerebral cortex during natural wake and sleep states. J. Neurosci. 19, 4595–4608.

Engel, A.K., Fries, P., Singer, W., 2001. Dynamic predictions: oscillations and synchrony in top-down processing. Nat. Rev. Neurosci. 2, 704–716.

Fries, P., 2005. A mechanism for cognitive dynamics: neuronal communication through neuronal coherence. Trends Cogn. Sci. 9, 474–480.

Harshman, R.A., 1972. Determination and proof of minimum uniqueness conditions for PARAFAC1.

Howard, M.W., Rizzuto, D.S., Caplan, J.B., Madsen, J.R., Lisman, J., et al., 2003. Gamma oscillations correlate with working memory load in humans. Cereb. Cortex 13, 1369–1374.

Jacobs, J., Kahana, M.J., 2009. Neural representations of individual stimuli in humans revealed by gamma-band electrocorticographic activity. J. Neurosci. 29, 10203–10214.

Jensen, O., Colgin, L.L., 2007. Cross-frequency coupling between neuronal oscillations. Trends Cogn. Sci. 11, 267–269.

Klausberger, T., Somogyi, P., 2008. Neuronal diversity and temporal dynamics: the unity of hippocampal circuit operations. Science 321, 53–57.

Kramer, M.A., Tort, A.B.L., Kopell, N.J., 2008. Sharp edge artifacts and spurious coupling in EEG frequency comodulation measures. J. Neurosci. Methods 170, 352–357.

Kruskal, J.B., 1976. More factors than subjects, tests and treatments—indeterminacy theorem for canonical decomposition and individual-differences scaling. Psychometrika 41, 281–293.

Kruskal, J.B., 1977. 3-way arrays—rank and uniqueness of trilinear decompositions, with applications to arithmetic complexity and statistics. Linear Alg. Appl. 18, 95–138.

Lachaux, J.P., Rodriguez, E., Martinerie, J., Varela, F.J., 1999. Measuring phase synchrony in brain signals. Hum. Brain Mapp. 8, 194–208.

Lakatos, P., Shah, A.S., Knuth, K.H., Ulbert, I., Karmos, G., Schroeder, C.E., 2005. An oscillatory hierarchy controlling neuronal excitability and stimulus processing in the auditory cortex. J. Neurophysiol. 94, 1904–1911.

Lakatos, P., Karmos, G., Mehta, A.D., Ulbert, I., Schroeder, C.E., 2008. Entrainment of neuronal oscillations as a mechanism of attentional selection. Science 320, 110–113.

Lancaster, J.L., Woldorff, M.G., Parsons, L.M., Liotti, M., Freitas, C.S., et al., 2000. Automated Talairach Atlas labels for functional brain mapping. Hum. Brain Mapp. 10, 120–131.

Le Van Quyen, M., Foucher, J., Lachaux, J.P., Rodriguez, E., Lutz, A., et al., 2001. Comparison of Hilbert transform and wavelet methods for the analysis of neuronal synchrony. J. Neurosci. Methods 111, 83–98.

Leurgans, S.E., Ross, R.T., Abel, R.B., 1993. A decomposition for 3-way arrays. SIAM J. Matrix Anal. Appl. 14, 1064–1083.

Lisman, J.E., Idiart, M.A.P., 1995. Storage of $7+/-2$ short-term memories in oscillatory subcycles. Science 267, 1512–1515.

Lord, F.M., Novick, M.R., 1968. Statistical theories of mental test scores. Addison-Wesley, Reading.

Maldjian, J.A., Laurienti, P.J., Kraft, R.A., Burdette, J.H., 2003. An automated method for neuroanatomic and cytoarchitectonic atlas-based interrogation of fMRI data sets. NeuroImage 19, 1233–1239.

Miwakeichi, F., Martinez-Montes, E., Valdes-Sosa, P.A., Nishiyama, N., Mizuhara, H., Yamaguchia, Y., 2004. Decomposing EEG data into space–time–frequency components using Parallel Factor Analysis. NeuroImage 22, 1035–1045.

Mocks, J., 1988. Decomposing event-related potentials—a new topographic components model. Biol. Psychol. 26, 199–215.

Mormann, F., Fell, J., Axmacher, N., Weber, B., Lehnertz, K., et al., 2005. Phase/amplitude reset and theta–gamma interaction in the human medial temporal lobe during a continuous word recognition memory task. Hippocampus 15, 890–900.

Morup, M., Hansen, L.K., Herrmann, C.S., Parnas, J., Arnfred, S.M., 2006. Parallel Factor Analysis as an exploratory tool for wavelet transformed event-related EEG. NeuroImage 29, 938–947.

Raghavachari, S., Kahana, M.J., Rizzuto, D.S., Caplan, J.B., Kirschen, M.P., et al., 2001. Gating of human theta oscillations by a working memory task. J. Neurosci. 21, 3175–3183.

Raghavachari, S., Lisman, J.E., Tully, M., Madsen, J.R., Bromfield, E.B., Kahana, M.J., 2006. Theta oscillations in human cortex during a working-memory task: evidence for local generators. J. Neurophysiol. 95, 1630–1638.

Rizzuto, D.S., Madsen, J.R., Bromfield, E.B., Schulze-Bonhage, A., Seelig, D., et al., 2003. Reset of human neocortical oscillations during a working memory task. Proc. Natl. Acad. Sci. U. S. A. 100, 7931–7936.

Schack, B., Vath, N., Petsche, H., Geissler, H.G., Moller, E., 2002. Phase-coupling of theta-gamma EEG rhythms during short-term memory processing. Int. J. Psychophysiol. 44, 143–163.

Schanze, T., Eckhorn, R., 1997. Phase correlation among rhythms present at different frequencies: spectral methods, application to microelectrode recordings from visual cortex and functional implications. Int. J. Psychophysiol. 26, 171–189.

Schroeder, C.E., Lakatos, P., 2009. Low-frequency neuronal oscillations as instruments of sensory selection. Trends Neurosci. 32, 9–18.

Sederberg, P.B., Kahana, M.J., Howard, M.W., Donner, E.J., Madsen, J.R., 2003. Theta and gamma oscillations during encoding predict subsequent recall. J. Neurosci. 23, 10809–10814.

Sidiropoulos, N.D., Bro, R., 2000. On the uniqueness of multilinear decomposition of N-way arrays. J. Chemometr. 14, 229–239.

Sirota, A., Montgomery, S., Fujisawa, S., Isomura, Y., Zugaro, M., Buzsaki, G., 2008. Entrainment of neocortical neurons and gamma oscillations by the hippocampal theta rhythm. Neuron 60, 683–697.

Sternberg, S., 1966. High-speed scanning in human memory. Science 153, 652–654.

Talairach, J., Tournoux, P., 1988. Co-planar stereotaxic atlas of the human brain. Thieme, Stuttgart, Germany.

Tort, A.B.L., Kramer, M.A., Thorn, C., Gibson, D.J., Kubota, Y., et al., 2008. Dynamic cross-frequency couplings of local field potential oscillations in rat striatum and hippocampus during performance of a T-maze task. Proc. Natl. Acad. Sci. U. S. A. 105, 20517–20522.

van Vugt, M.K., Schulze-Bonhage, A., Sekuler, R., Litt, B., Brandt, A., et al., 2009. Intracranial electroencephalography reveals two distinct similarity effects during item recognition. Brain Res. 1299, 33–44.

van Vugt, M.K., Schulze-Bonhage, A., Litt, B., Brandt, A., Kahana, M.J., 2010. Hippocampal gamma oscillations increase with memory load. J. Neurosci. 30, 2694–2699.

Varela, F., Lachaux, J.P., Rodriguez, E., Martinerie, J., 2001. The brainweb: phase synchronization and large-scale integration. Nat. Rev. Neurosci. 2, 229–239.

von Stein, A., Sarnthein, J., 2000. Different frequencies for different scales of cortical integration: from local gamma to long range alpha/theta synchronization. Int. J. Psychophysiol. 38, 301–313.

von Stein, A., Chiang, C., Konig, P., 2000. Top-down processing mediated by interareal synchronization. Proc. Natl. Acad. Sci. U. S. A. 97, 14748–14753.